AXIAL-SCAN FLUORESCENCE FLUCTUATION SPECTROSCOPY: INITIAL DEVELOPMENT AND EXPERIMENTAL CHALLENGES

A THESIS
SUBMITTED TO THE FACULTY OF THE GRADUATE SCHOOL
OF THE UNIVERSITY OF MINNESOTA
BY

YUN CHEN

IN PARTIAL FULFILLMENT OF THE REQUIREMENTS
FOR THE DEGREE OF
MASTER OF SCIENCE

ADVISOR: JOACHIM MUELLER

MAY 2010

Acknowledgements

I would like to express my appreciation to my advisor, Joachim Mueller, who supervised my research.

Dedication

This thesis is dedicated to my parents who always believe in my ability.

Table of Contents

List of Figures

List of Abbreviations

FFS	Fluorescence Fluctuation Spectroscopy
FCS	Fluorescence Correlation Spectroscopy
ACF	Autocorrelation Function
PCH	Photon Counting Histogram
PSF	Point Spread Function
3DG	3-dimenional Gaussian
GL	Gaussian Lorentzian
GFP	Green Fluorescent Protein
APD	Avalanche Photon Diode

CHAPTER I INTRODUCTION TO AXIAL-SCAN FLUORESCENCE FLUCTUATION SPECTROSCOPY

1.1 Motivation

Quantification of protein-protein interactions inside living cells is a prerequisite for the development of an accurate picture of cellular pathways on the molecular level. Such information is also a prerequisite for the development of quantitative and physical models of biological processes. As an example, consider the assembly of a virus particle in a cell, which involves the coordinated assembly of thousands of proteins. Many details of the viral assembly process inside cells are currently only poorly understood [1-4]. The active transport of cargo proteins across the nuclear membrane by transport factors is another open question [5]. The mechanism by which transport factors achieve selective translocation through the nuclear pore complex is not yet established, but interactions between transport factors and nucloeporins are thought to play an important role [6]. While we currently lack a well-established technique that quantifies protein interactions in cells, a method called fluorescence fluctuation spectroscopy (FFS) is emerging that promises to determine the binding curve and stoichiometry of protein-protein interactions in the living cell [7-9].

FFS relies on fluorescently tagged proteins and detects the formation of protein complexes by an enhancement of the brightness, which is an FFS parameter representing the intensity of a fluorescent particle. For example, the brightness of a dimeric protein complex is twice that of a monomeric protein. The FFS technique relies on a small optical observation volume, which gives rise to signal fluctuations as fluorescent proteins move in and out of this volume. FFS theory implicitly assumes that the optical observation volume is completely enclosed by the sample reservoir. This assumption is reasonable for FFS measurements in the cell nucleus, which is typically the thickest part of the cell. However, this assumption is problematic for cell measurements in the cytoplasm or at membranes, where the thickness of the sample is less than that of the observation volume. Thus, many interesting applications of FFS to processes that occur

in the cytoplasm or at membranes are currently not feasible. As a consequence most FFS studies have been limited to the cell nucleus.

Viral assembly and nucleocytoplasmic transport involve protein processes in the cytoplasm and at membranes. In order to study these systems by FFS methods we explore in this thesis the application of FFS to thin samples. We first establish that thin samples indeed introduce a significant bias into the brightness measurement by FFS. To address this problem, we performed scans along the axial direction of the beam and developed an FFS model that takes the finite height of the cell into account. We show that the axial-scan method is a promising approach to incorporate the finite thickness of the samples into FFS measurements. As proof-of-principle we determine the brightness of a green fluorescent protein in thick and thin sections of the cell. We encountered a couple of technical challenges and describe their solutions. Recently, we realized that the instrument suffers from mechanical drifts, which prohibits accurate FFS measurement across the axial profile of the cell. This introduces a serious limitation into the method and needs to be overcome before axial-scan FFS can be applied to biological systems.

This thesis describes the theoretical and experimental development of axial-scan two-photon FFS and the introduction of a modified brightness analysis to study cytoplasmic protein interactions. The thesis should also serve as a starting point for the further development of the technique into a robust and quantitative tool with many potential biophysical applications in cells.

1.2 Fluorescence Fluctuation Spectroscopy (FFS)

FFS extracts information about the dynamics and interactions of diffusing macromolecules such as proteins from the fluorescence fluctuations of a small optical observation volume within the sample [10, 11]. Two-photon FFS, a combination of 2-photon excitation and FFS, creates a very small optical observation volume ($V < 1$ fl) and at the same time eliminates out-of-focus photo bleaching [12], which is beneficial for intracellular measurements. A well known analytic method is fluorescence correlation spectroscopy (FCS) that calculates the autocorrelation function (ACF) of the signal variations due to

fluorescent molecules diffusing through a small optical observation volume [11, 13]. While the ACF contains information about the diffusion process of molecules, a mixture of two or more species with similar molecular weights cannot be resolved by FCS [14]. A second analysis method, photon counting histogram (PCH), was introduced to fill this gap by resolving molecular species based on their intrinsic brightness, not by their diffusion properties [15]. Brightness is defined as the average photon counts detected per fluorescent molecule per sampling time. Supposed we are interested in the oligomerization of protein A, we will genetically attach one fluorescent tag of brightness λ to each protein A. If protein A is non-interacting, the brightness detected of each fluorescently tagged protein A will be λ. If protein A exists as a homo-dimer, it will display a brightness of 2λ, because the protein complex contains two fluorescent labels. Since PCH detects the brightness increase when proteins associate to form complexes, it is a sensitive tool to quantify protein interactions [7, 10].

So far, most quantitative applications of FFS in cells by our [7, 15] group have been confined within the nucleus. Moving out of the nucleus into the cytoplasm and to the membrane faces experimental challenge due to the geometry of the sample. If not taken into account, the finite size of cellular compartments is able to introduce significant biases into the analysis of data and thereby destroy the quantitative character of FFS experiments. For example, brightness has been introduced as a quantitative marker of protein oligomerization [8]. Currently this method cannot be applied to study oligomerization processes in the cytoplasm or on membranes because of the influence of sample size on FFS parameters. We aimed to incorporate the geometry of the sample into FFS experiments and modify brightness analysis for such cases.

1.2.1 Sample Geometry Function $S(\mathbf{r})$

FFS collects the fluctuating fluorescence intensity $F(t)$ of molecules moving through an optical observation volume. If only a single fluorescent species is present in the sample region, the fluorescence intensity detected is [16]

$$F(t) = \lambda \int PSF(\mathbf{r}) C(\mathbf{r}, t)\, d\Omega \tag{1.1}$$

λ is defined as the brightness per molecule per second; it contains the information of the absorptivity, fluorescence quantum efficiency, and the fluorescence collection efficiency of the instrument; $C(\mathbf{r},t)$ is the concentration of fluorescent molecules at position $\mathbf{r}$ and at time t. *PSF* denotes the point spread function, which describes the shape of the excitation light and the sample geometry

$$PSF(\mathbf{r}) = \left(\frac{I(\mathbf{r})}{I(0)} \right)^n S(\mathbf{r}), \tag{1.2}$$

where $I(\mathbf{r})$ is the intensity of the excitation light at position $\mathbf{r}$ and n identifies n-photon excitation. The function $S(\mathbf{r})$ describes the sample geometry; $S(\mathbf{r}) = 1$ if position $\mathbf{r}$ is accessible to fluorophores, and is zero everywhere else. All FFS models and experiments in the literature assume an infinite sample size ($S(\mathbf{r}) = 1$). We introduce $S(\mathbf{r})$ to provide a method for extending FFS theory to finite sample geometry. A good part of the paper will be devoted to exploring the consequences of introducing $S(\mathbf{r})$.

Under equilibrium conditions, molecules are uniformly distributed, which is characterized by a time- and space-independent average concentration C. Fluctuations of the concentration around its mean lead to fluctuations of the fluorescence intensity

$$\delta F = F(t) - \langle F \rangle, \tag{1.3}$$

where the average fluorescence intensity is given by

$$\langle F \rangle = \lambda C \int PSF(\mathbf{r}) d\Omega \tag{1.4}$$

1.2.2 Analysis Methods

FCS, PCH and moment analysis are useful tools for analyzing FFS data and characterizing different physical quantities of the sample. While each analysis method provides unique information, there is also considerable overlap. Here, we briefly highlight the fundamental concepts of the analysis methods that are needed for describing our experimental data.

For sake of simplicity let us consider a sample with a single fluorophore species. The fluorescence intensity $F(t)$ is a directly measurable quantity. Its first moment is the

average fluorescence intensity $\langle F \rangle$. In PCH, $\langle F \rangle$ is reinterpreted as the product of N_{PSF} (the average number of fluorescent molecules inside the focal volume V_{PSF}) and the brightness (average photon count rate per second) per molecule λ.

$$\langle F \rangle = \lambda N_{PSF} \tag{1.5}$$

The average number of photons detected per sampling time is

$$\langle k \rangle = \langle F \rangle \cdot T , \tag{1.6}$$

with T being the sampling time.

In the FFS literature, the average photon counts is expressed as

$$\langle k \rangle = \varepsilon N_{PSF} , \tag{1.7}$$

where

$$\varepsilon = \lambda T . \tag{1.8}$$

ε is referred to as the brightness per sampling time of a molecule. It is the average number of photons detected from a single molecule during the sampling time T.

The focal volume is defined in the following form.

$$V_{PSF} \equiv \int PSF d\Omega \tag{1.9}$$

The average number of fluorescent molecules inside the focal volume is simply the product of the concentration and the volume.

$$N_{PSF} = CV_{PSF} \tag{1.10}$$

After considering the average value of $F(t)$, we now turn to fluctuations. FCS defines the ACF of the fluorescence intensity as

$$\begin{aligned} G(\tau) &= \frac{\langle \delta F(t+\tau) \delta F(t) \rangle}{\langle F(t) \rangle^2} \\ &= \frac{\langle F(t+\tau) F(t) \rangle - \langle F \rangle^2}{\langle F \rangle^2} \end{aligned} \tag{1.11}$$

If we use Eq.(1.4) and assume that the fluorescence solution is so dilute that fluorescent molecules are not interacting with each other, the zero time correlation function

$$G(0) = \frac{\langle \delta F \delta F \rangle}{\langle F \rangle^2} \tag{1.12}$$

reduces to

$$G(0) = \frac{\int PSF^2 d\Omega}{C\left(\int PSF d\Omega\right)^2} \tag{1.13}$$

By introducing a gamma factor that contains information about the shape of the sample as well as the shape of the excitation light,

$$\gamma_{PSF} = \frac{\int PSF^2 d\Omega}{\int PSF\, d\Omega} \tag{1.14}$$

the fluctuation amplitude $G(0)$ is written in the following form.

$$G(0) = \frac{\gamma_{PSF}}{N_{PSF}} \tag{1.15}$$

The ACF (1.10) is the product of the fluctuation amplitude $G(0)$ and a time-dependent function $g(\tau)$, which depends on the diffusion coefficient and the *PSF* [16]. In the following we will only consider the fluctuation amplitude $G(0)$. Another important quantity is Mandel's Q factor. It is the ratio of the variance to the mean of the fluorescence signal [15, 17]

$$Q = \frac{\langle \delta k \delta k \rangle - \langle k \rangle}{\langle k \rangle} \tag{1.16}$$

We assume throughout this paper that the undersampling effect is negligible [18, 19]. In other words, the photon count fluctuations track the instantaneous fluorescence intensity fluctuations. With the help of Eq. (1.12). Mandel's Q parameter is expressed as the product of the zero time ACF and the average fluorescence intensity.

$$Q = G(0) \cdot \langle k \rangle \tag{1.17}$$

By inserting Eqs. (1.7) and (1.15) the Q parameter is written as the product of the brightness and the gamma factor.

$$Q = \varepsilon \cdot \gamma_{PSF} \tag{1.18}$$

We experimentally obtain the values for the average fluorescence intensity and Mandel's Q factor. They both are functions of ε (or λ), C and PSF. If the point spread function is known, the brightness and the concentration can be calculated.

CHAPTER II: STATEMENT OF THE PROBLEM AND NEW EXPERIMENTAL APPROACH

2.1 Sample Size and Observation Volume

FFS experiments are usually carried out inside a sample that is much larger than the focal volume (~1 fl). The most common sample configuration is a well containing a fluorescent solution of ~ 0.5 ml. We refer to this situation as the infinite sample case with the point spread function given by

$$PSF_{\infty} = \left(\frac{I(\mathbf{r})}{I(0)} \right)^{n} \cdot 1 \tag{1.19}$$

where $S(\mathbf{r}) = 1$, the subscript denotes an infinite sample.

The assumption of an infinite sample is problematic when considering cellular FFS experiments, in which part of the excitation volume resides outside of the sample and excites no fluorophore (Fig1).

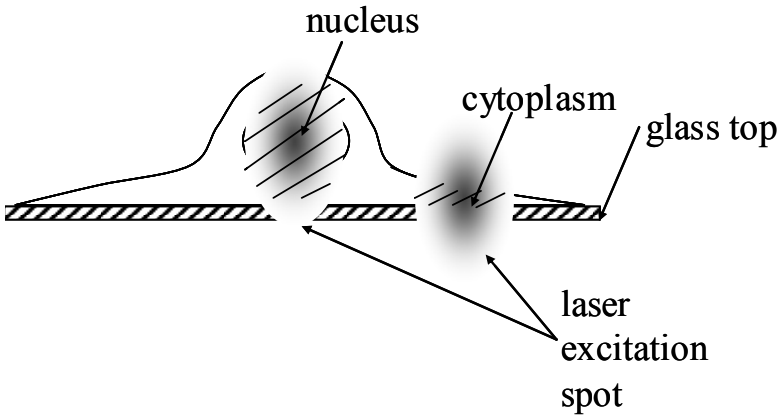

FIGURE 1 Excitation volume and a cell

The cartoon shows our experimental setup, in which a cell sits on top of a petri dish. The laser beam is focused at the center of the cell nucleus and the center of cytoplasm respectively. The hatched area is the overlap of the excitation volume and the sample

We found experimentally that measurements in the cytoplasm of the cell are usually not described by the infinite sample approximation. In fact, only the cell nucleus is thick enough that the infinite sample approximation holds. As an experimental test we transfected cells with the green fluorescent protein (GFP) and determined its brightness at different locations within the cell using conventional FFS analysis. It is well established that GFP is a monomeric protein. Thus we expect to recover the same brightness irrespective of position. However, we find cases where the brightness of green fluorescent protein (GFP) in the cytoplasm is apparently higher than the brightness measured in the nucleus (Fig. 2). The apparent increase in brightness correlates with the sample thickness. A reduction in the cell thickness leads to an increase in brightness. , we would erroneously conclude that the protein dimerizes at thin cytoplasmic sections of the cell. Conventional FFS analysis introduces a brightness bias which leads to erroneous conclusions about protein interactions.

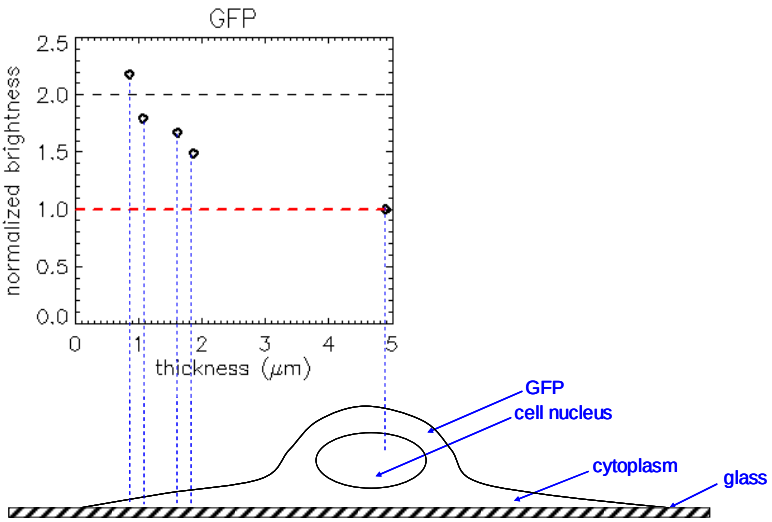

FIGURE 2. Conventional brightness analysis at different positions of a cell The upper graph shows the brightness (diamond) measured at the center of different cellular sections. The red dash line is the expected brightness of a monomer GFP and the black dash line is the expected brightness of a dimeric GFP. The brightness at cytoplasmic sections is apparently high than at the nucleus.

2.2 Z-scan FFS

To obtain an unbiased analysis of the protein interaction at thin cell cytoplasmic sections, we need to consider the effect of the size of the sample. However, we do not know beforehand the size of the cytoplasm which varies across the cell. Neither do we know the exact position of our excitation beam relative to the cytoplasm. To address these two difficulties, we introduce z-scan FFS.

2.2.1 The Idea

The concept of z-scan FFS is illustrated in Fig. 3. Let's consider a thin slab sample of height *h*. We scan the focus of the excitation light along the z-axis which is perpendicular to the thin sample. At selected steps of the z-scan we perform FFS

measurements. The overlap between the beam and the sample changes systematically for each measurement and provides information about the shape and size of the sample.

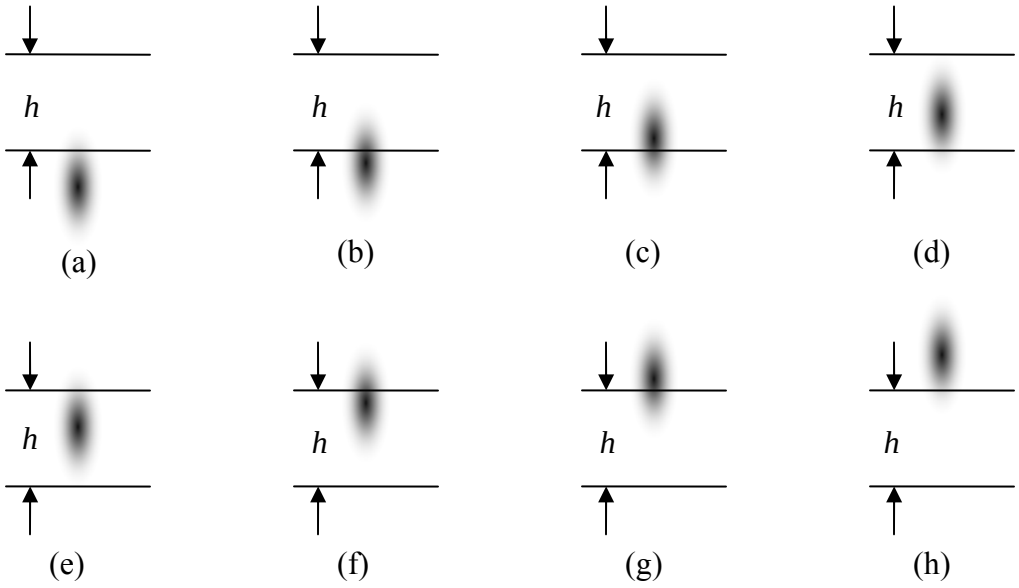

FIGURE 3. Illustration of the Z-scan FFS concept

The beam focus goes across the sample along the axial direction (z direction). (a)-(h) are different positions of the beam focus relative to the sample.

We model the cytoplasmic sections enclosed by the observation volume as fluorescent slabs based on our experimental setup. The plane of the coverslip lies in the x-y plane with the optical axis along z (Fig. 4). The diameter of a typical COS cell is ~ 50 μm in the x-y plane with a thickness that decreases from the center (~ 5 μm) to the periphery. The intensity of the excitation light is azimuthally symmetric. The axial direction is parallel to z, and the radial direction lies in the x-y plane. Compared with the size of the cell along the x-y plane, the radial beam waist (~ 0.5 μm) of the excitation light is small enough that the change in thickness of the cytoplasm section within the

excitation light is negligible. Therefore, we model the cytoplasm section as a slab of constant height.

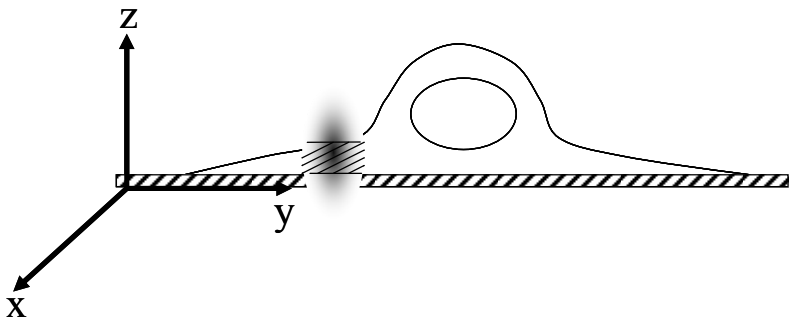

FIGURE 4. Experimental configuration of the cell and the excitation beam
The grey spot indicates the focus of the excitation light, and the hatched area enclosed by the excitation light is the cytoplasm section approximated as a slab.

2.2.2. Point Spread Function (PSF)

Since conventional FFS theory based on an infinite sample is invalid for samples with finite geometry, our first task is to develop a model for analyzing FFS parameters of a slab sample with height h. The geometrical parameters and relations required for the model are shown in Fig. 5. Distances are measured with reference to an arbitrary reference point defining the origin. The bottom membrane and top membrane are located at height h_0 and $h_0 + h$, respectively.

The center of the excitation light is marked by position z as shown in Fig. 5. The function $S(\mathbf{r})$ describes the restricted geometry of the sample. For a slab with height h, the shape factor is

$$S(\mathbf{r}) = \begin{cases} 1, & h_0 < z < h_0 + h \\ 0, & \text{otherwise} \end{cases} \tag{1.20}$$

where h_0 marks the starting position of the sample.

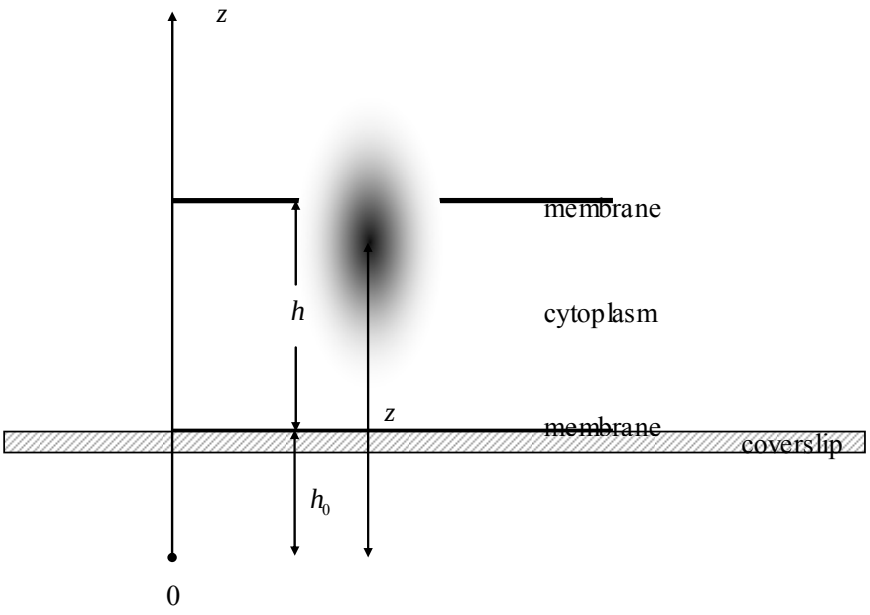

FIGURE 5 Z-scan across the cytoplasm section of a cell

The starting point of the scan is arbitrary. We choose the starting point as the origin of the z axis. The distance between the origin and the lower membrane is h_0; the distance from the origin to the center of the excitation light is z; the local thickness of the cytoplasm section enclosed by the two membranes is h.

The modeling of fluorescence intensity in Eq. (1.4) and its fluctuation in Eq. (1.18) requires a wise choice of the PSF. Our PSF (1.2) is made up of two parts: the sample size and the intensity distribution of the laser beam.

The intensity distribution of a laser focus spot is frequently described by a 3D Gaussian model or a Gaussian-Lorentzian model [20].

3D Gaussian Model

The 3D Gaussian (3DG) model describes the laser intensity along the azimuthally symmetric direction with a Gaussian function and the laser intensity on each plane perpendicular to the axial axis with another Gaussian function,

$$I(\mathbf{r}) = I_0 \exp\left(-\frac{2z^2}{z_0^2} - \frac{2\left(x^2+y^2\right)}{r_0^2} \right) \tag{1.21}$$

where z_0 and r_0 are beam waists along and perpendicular to the axial axis. The corresponding PSF for two photon excitation is

$$PSF(\mathbf{r}) = \exp\left(-\frac{4z^2}{z_0^2} - \frac{4\left(x^2+y^2\right)}{r_0^2} \right) S(\mathbf{r}) \tag{1.22}$$

When the observation volume is at an arbitrary position z as in Fig. 5., both the observation volume and the gamma factor can be obtained through integrating different powers of the PSF .

$$V(z) = \frac{\pi\sqrt{\pi}}{16} r_0^2 z_0 \left(\mathrm{Erf}\left(2\left(h - z + h_0\right)/z_0\right) + \mathrm{Erf}\left(2\left(z - h_0\right)/z_0\right) \right) \tag{1.23}$$

$$\gamma(z) = \frac{1}{2\sqrt{2}} \frac{\mathrm{Erf}\left(2\sqrt{2}\left(h - z + h_0\right)/z_0\right) + \mathrm{Erf}\left(2\sqrt{2}\left(z - h_0\right)/z_0\right)}{\mathrm{Erf}\left(2\left(h - z + h_0\right)/z_0\right) + \mathrm{Erf}\left(2\left(z - h_0\right)/z_0\right)} \tag{1.24}$$

where Erf is the error function, h is the thickness of the sample, h_0 is the offset between the bottom of the slab sample and the starting point of the scan, and z is the position of the center of the excitation beam.

The fluorescence intensity is the product of the observation volume, the average brightness per second λ and the concentration C of the fluorophore.

$$\left\langle F(z) \right\rangle = \frac{\pi\sqrt{\pi}}{16} r_0^2 z_0 \lambda C \left(\mathrm{Erf}\left(2\left(h - z + h_0\right)/z_0\right) + \mathrm{Erf}\left(2\left(z - h_0\right)/z_0\right) \right) + B \tag{1.25}$$

where B is the background fluorescence which can be controlled to be much smaller than the signal.

The Mandel's Q parameter, which shows the fluctuation of the fluorescence intensity, is the product of the brightness per sampling time ε and the gamma factor

$$Q(z)=\frac{\varepsilon}{2\sqrt{2}}\frac{\mathrm{Erf}\left(2\sqrt{2}\left(h-z+h_0\right)/z_0\right)+\mathrm{Erf}\left(2\sqrt{2}\left(z-h_0\right)/z_0\right)}{\mathrm{Erf}\left(2\left(h-z+h_0\right)/z_0\right)+\mathrm{Erf}\left(2\left(z-h_0\right)/z_0\right)} \tag{1.26}$$

In the infinite sample case where we subscript the parameters with $3DG,\infty$, we get the following expressions for the observation volume, gamma factor, fluorescence intensity and the Q parameters:

$$V_{3DG,\infty}=\frac{\pi\sqrt{\pi}\omega_0^2 z_0}{8} \tag{1.27}$$

$$\gamma_{3DG,\infty}=\frac{1}{2\sqrt{2}} \tag{1.28}$$

$$F_{3DG,\infty}=\lambda C V_{3DG,\infty} \tag{1.29}$$

$$Q_{3DG,\infty}=\frac{\varepsilon}{2\sqrt{2}} \tag{1.30}$$

Gaussian-Lorentzian Model

Another model commonly in use is the Gaussian-Lorentzian (GL) model, which has the following mathematical expression for its beam profile.

$$I(\mathbf{r})=\frac{I_0\omega_r^2}{\omega^2(z)}\exp\left(-\frac{2r^2}{\omega^2(z)}\right) \tag{1.31}$$

where I_0 is the peak intensity, ω_r is the radial beam waist, z_r is the axial beam waist, and

$$\omega^2(z)=\omega_r^2\left(1+\left(\frac{z}{z_r}\right)^2\right) \qquad z_r=\frac{\pi\omega_r^2}{\lambda} \tag{1.32}$$

where λ is the wavelength of the excitation beam. The PSF for two-photon excitation is

$$PSF(\mathbf{r})=\frac{\omega_r^4}{\omega^4(z)}\exp\left(-\frac{4r^2}{\omega^4(z)}\right)S(\mathbf{r}) \tag{1.33}$$

The fluorescence intensity and the Q parameter for the slab configuration shown in Fig. 5 are calculated,

$$\langle F \rangle = \frac{\lambda C \pi z_r^2}{4}\left(\arctan\left(\left(h - z + h_0\right)/z_r\right) + \arctan\left(\left(z - h_0\right)/z_r\right)\right) + B \tag{1.34}$$

where λ and B are defined as the same through out this thesis.

$$Q(z) = \frac{1}{16}\left(\frac{\dfrac{5\dfrac{h-z+h_0}{z_r} + 3\left(\dfrac{h-z+h_0}{z_r}\right)^3}{\left(1+\left(\dfrac{h-z+h_0}{z_r}\right)^2\right)^2} + \dfrac{5\dfrac{z-h_0}{z_r} + 3\left(\dfrac{z-h_0}{z_r}\right)^3}{\left(1+\left(\dfrac{z-h_0}{z_r}\right)^2\right)^2}}{\arctan\left(\dfrac{h-z+h_0}{z_r}\right) + \arctan\left(\dfrac{z-h_0}{z_r}\right)} \right) \tag{1.35}$$

The subscript GL,∞ will be used for all quantities that refer to an infinite sample with GL excitation profile. According to Eq. (1.9), the point spread function volume is calculated as

$$V_{GL,\infty} = \frac{\pi^2 \omega_r^2 z_r}{4} \tag{1.36}$$

The number of fluorescent molecules inside the point spread function volume is obtained by using Eq. (1.10).

$$N_{GL,\infty} = \frac{\pi^2 \omega_r^2 z_r C}{4} \tag{1.37}$$

If we assume that the brightness does not change with sample size, the average photon counts is

$$\langle F \rangle_{GL,\infty} = \frac{\pi^2 \omega_r^2 z_r \lambda C}{4}, \tag{1.38}$$

the gamma factor is

$$\gamma_{GL,\infty} = \frac{3}{16}, \tag{1.39}$$

the zero-time correlation amplitude is

$$G(0)_{GL,\infty} = \frac{3}{4C\pi^2\omega_r^2 z_r}, \tag{1.40}$$

and the Mandel's Q factor is

$$Q_{GL,\infty} = \frac{3\varepsilon}{16} \tag{1.41}$$

2.3 Experimental Results

2.3.1 Experimental Setup

The experimental setup is shown in Fig. 6. Ultra short pulses (~100 fs) are generated by a mode-locked Ti:sapphire laser (Tsunami, Spectra-Physics, Mountain View, CA), which is pumped by a diode pumped, cw laser (Millennia Vs, Spectra-Physics). The repetition frequency of the laser pulses is 80 MHz. The laser beam enters a Zeiss Axiovert 200 microscope (Zeiss, Gottingen, Germany). A Zeiss objective (either Plan-Apochromat 63x oil immersion objective (N.A.= 1.4) or C-Apochromat 63x water immersion objective (N.A.= 1.2)) focuses the incoming laser light to generate a high photon flux at the focus. The fluorescence signal from two-photon absorption of the sample is collected by the objective and detected by an avalanche photon diode (APD, model SPCM-AQR-14, Perkin Elmer, Vaudreuil, Canada). Fluorescence intensity is measured in photon counts per second (cps) and recorded by an FCS data acquisition card (ISS, Champaign, IL). The power after either the oil or water immersion objective is controlled to be 0.20-0.24 mW and the data acquisition frequency is 20 kHz for cell measurements. In dye solution measurements, the power after the objective is 1.3-1.5 mW with a sampling frequency of 50 kHz. All experiments are performed with a laser wavelength of 905 nm. A dichroic beam splitter #1 (675DCSXR, Chroma Technology Corp., Brattleboro, VT) reflects light with a wavelength above 700 nm and transmits those of shorter wavelengths. In our experimental setup, the 905 nm excitation light is reflected by filter #1 and excites the sample. The fluorescence emission of GFP covers wavelengths from ~500 nm to 550 nm and passes through filter #1. The dichroic filter #2 (FF01-750/SP, Semrock, Rochester, NY) acts as a blocking filter eliminating residual laser light, while passing the visible spectrum. Laser power is measured after the

objective. For cell measurements its value is always less than 1 mW in order to avoid bleaching of GFP.

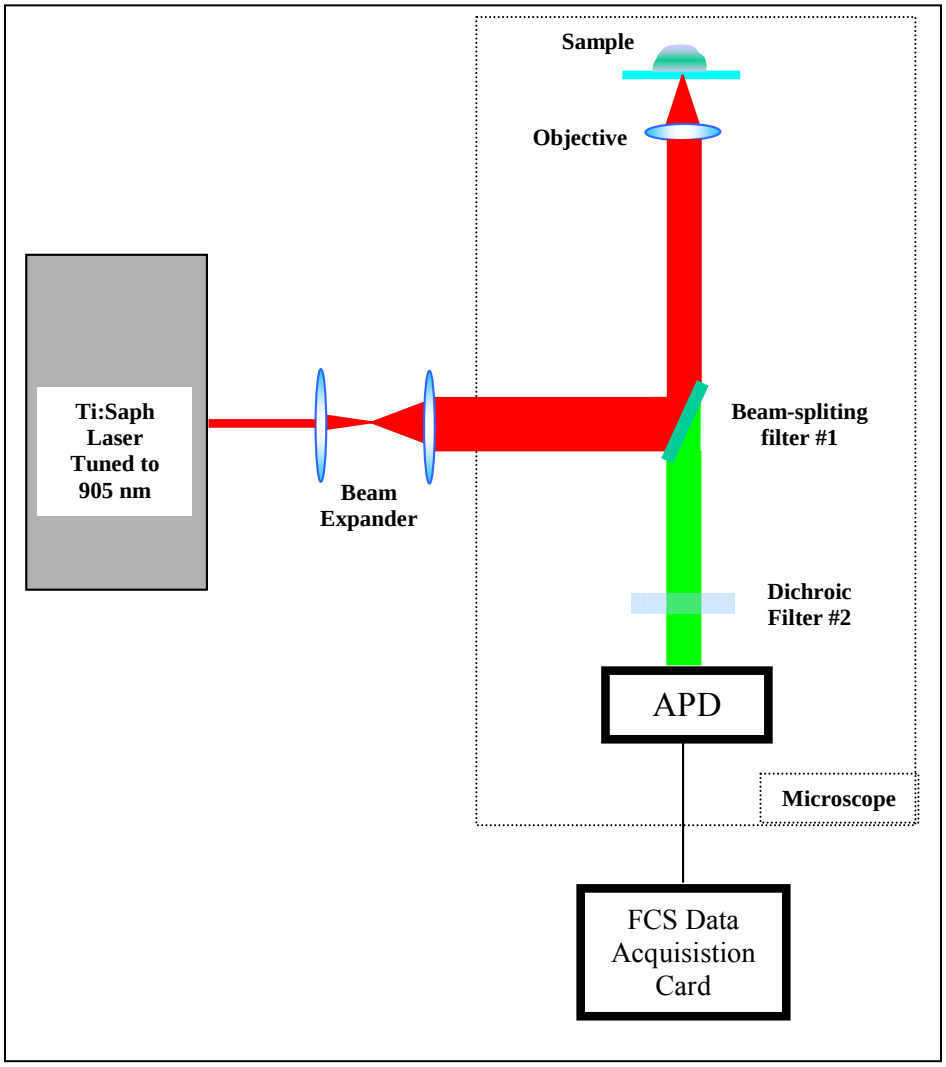

FIGURE 6 Schematic diagram of two-photon instrument.

2.3.2 Sample Preparation

COS cells obtained from ATCC (Manassas, VA) are maintained in 10% fetal bovine serum (Hyclone Laboratories, Logan, UT) and DMEM media. Cells were subcultured in eight-well coverglass chamber slides (Nalge Nunc International, Rochester, NY). They were transfected using Polyfect (Qiagen, Valencia, VA) with GFP plasmid.

Before every measurement, the growth media was removed and replaced with phosphate buffered saline (PBS).

2.3.3 Initial Experimental Results Obtained by Z-scan FFS

We choose COS cells expressing GFP as our model system. GFP is found both in the cytoplasm and in the nucleus of transfected COS cells at equal concentration. Here we represent the results of z-scan FFS taken at the nucleus and the cytoplasm. By fitting the z-dependence profiles of the fluorescence intensity and Mandel's Q factor simultaneously to our modified FFS model we obtain the thickness of the cell at the position where the z-scan is performed, the brightness and the concentration of the protein.

Figs. 7 and 8 show the experimental data in the nucleus and the fits to different models. The fluorescence intensity is expressed in counts per second (cps) at every step of the scan along the thick part of the cell. The Q parameter is in counts per molecule per second (cpms). A fit to the 3DG model (Eq. (1.25) and (1.26)) determines the thickness of this section as h = 4.69 μm. The z-offset h_0, which is the distance between the starting point of the scan and the bottom edge of the sample, is 3.32 μm (Fig. 7). The fit to the GL model (Eq. (1.34) and (1.35)) returns the thickness as 4.68 μm and the offset as 3.32 μm (Fig. 8).

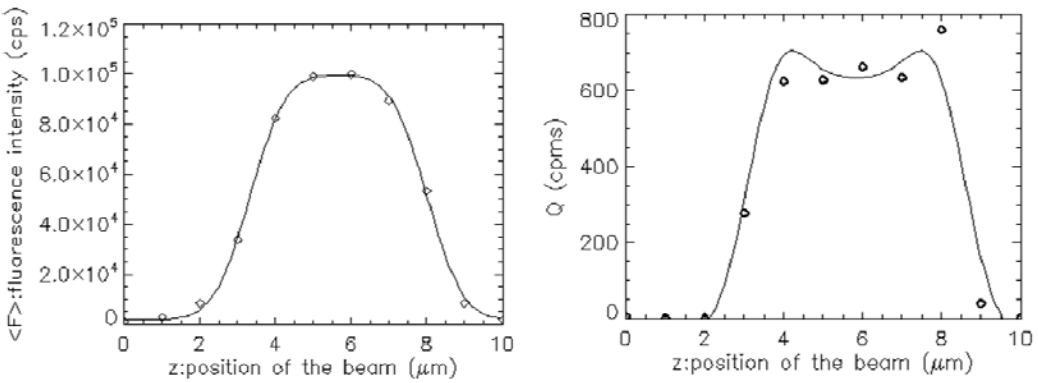

FIGURE 7 Z-scan profiles across the nucleus of a COS cell transfected with GFP are fitted with the 3DG model

On the left hand side is fluorescence intensity as a function of the axial beam position; on the right hand side is the Q parameter. The average intensity and Mandel's Q parameter (diamond) were measured for each step of the scan; they were fit simultaneously to a 3DG model (solid). The distance h_0 marks the difference between the origin of the scan (z = 0) and the bottom of the sample. The fit recovered an offset h_0 of 3.32 μm and a thickness of h = 4.69 μm.

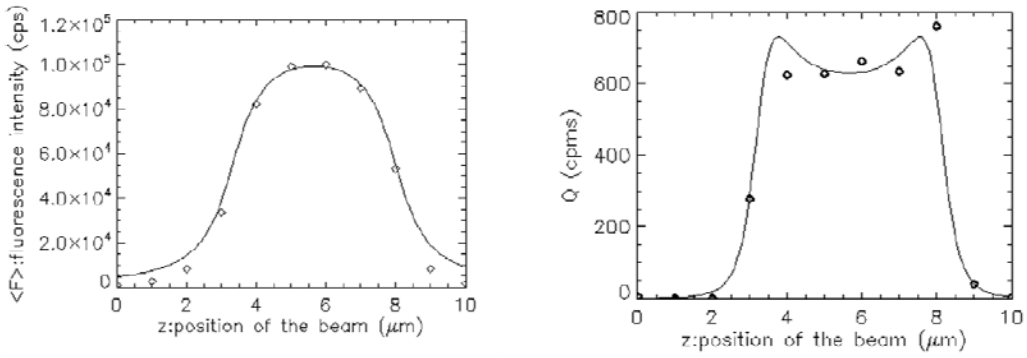

FIGURE 8 Z-scan profiles across the nucleus of a COS cell transfected with GFP are fitted with the GL model

The same data as in Fig. 7 are fit to another PSF model. The fluorescence intensity is on the left and the Q parameter is on the right. Both experimental quantities (diamonds) were fit simultaneously to a GL model (solid). The fit recovered an offset h_0 of 3.32 μm and a thickness of 4.68 μm.

We also axially scanned a thin cytoplasmic section of the same cell. Figs. 9 and 10 show the fluorescence intensity and Q parameter profiles as well as their fits using the two different PSF-models.

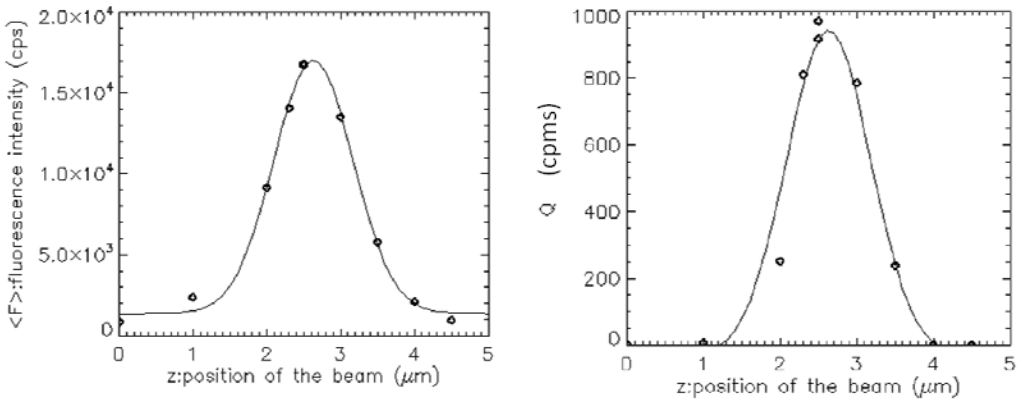

FIGURE 9 Z-scan profiles across the cytoplasm of a COS cell transfected with GFP are fitted with the 3DG model

The fluorescence intensity measured at each step of the scan is on the left and the Q parameter is on the right panel (diamonds). They were fit simultaneously to a 3DG model (solid). The fit returned an offset h_0 of 2.50 μm and a thickness of 0.26 μm.

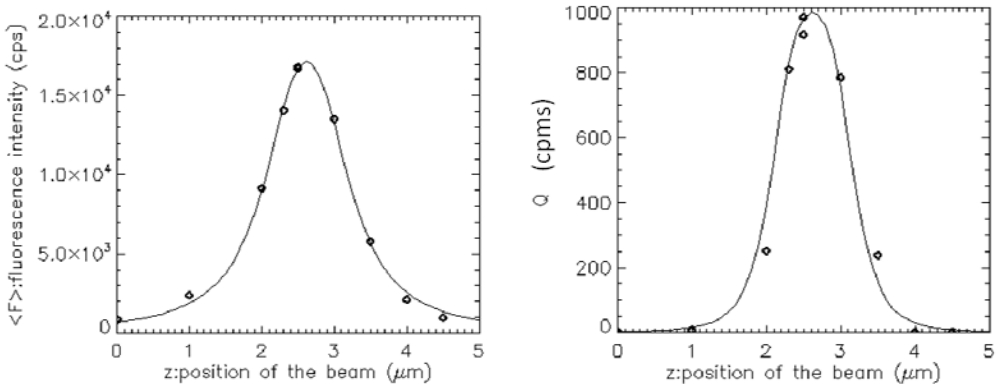

FIGURE 10 Z-scan profiles across the cytoplasm of a COS cell transfected with GFP are fitted with the GL model

The same data as in Fig. 9 are fit to a GL model (solid). The fit recovered an offset h_0 of 2.24 μm and a thickness of $z_0 = 0.76$ μm .

In Figs.7 and 8, the thickness of the sample from the fit to the 3DG model is 4.69 μm, which is within error identical to that from the fit to the GL model. This result is encouraging. However, the asymmetry of the experimental z-scan profiles is obvious. The expected peak of the Q parameter at the lower boundary of the sample does not show up. Our theory cannot account for the observed asymmetry. In Figs. 9 and 10, the asymmetric feature of in the cytoplasm data is not as strong as in the nucleus data, which is due to the fact that the cytoplasm section is much thinner than the nuclear one. The expected peaks of the Q parameters at the lower and upper boundaries of the cell are so close that they cannot be told apart. But the fitted thicknesses from both models do not agree with each other. The 3DG model returns a thickness of 0.26 μm; the GL model recovers a thickness of 0.76 μm.

In conventional FFS where the whole PSF is enclosed by the fluorescent sample, the difference between the GL and the 3DG model are usually negligible, because both models are generally successful to analyze correlation functions or photon counting histograms. However, in z-scan FFS, the fluorescence signal depends explicitly on the axial part of the PSF. For this reason z-scan FFS is significantly more sensitive to the axial shape of the PSF than conventional FFS experiments. We need to identify the proper PSF for precise analysis of data. In addition, theory predicts a symmetric z-scan profile for a slab sample, while our experimental data show an asymmetric scanning profile. These two points need to be addressed in our technique development. We first tackle the severe asymmetry of our data in the next chapter.

Chapter III SPHERICAL ABERRATION

3.1 Spherical Aberration

Spherical aberrations are departures of the performance of an optical system from the prediction of paraxial optics. Aberration blurs an image produced by an optical system. For example, a manufactured lens with a spherical surface focuses the propagating rays tighter when they are far from the optical axis as than they are close to the optical axis. In z-scan FFS experiments the refractive index mismatch can induce spherical aberrations that may lead to a focus-depth dependent degradation of resolution.

In our experiment setup (Fig. 11), the laser beam passes through oil which is the immersion medium of the objective, the bottom slide of the glass Petri dish, the cell and the saline solution which was used to maintain a suitable environment for cells. The objective (Zeiss 63x/1.4NA oil immersion objective) is used with 0.17 mm-thick glass slides to achieve the best imaging condition. However, the mismatch in the refractive index that occurs at the interface of the oil-cell and the cell-saline boundaries lead to changes in the directions of the propagating light rays. The incident angle of the light rays varies with distance from the optical axis. Each incident angle will be refracted by a different degree. This refraction leads to a degradation of the focus spot, which depends on the focusing depth.

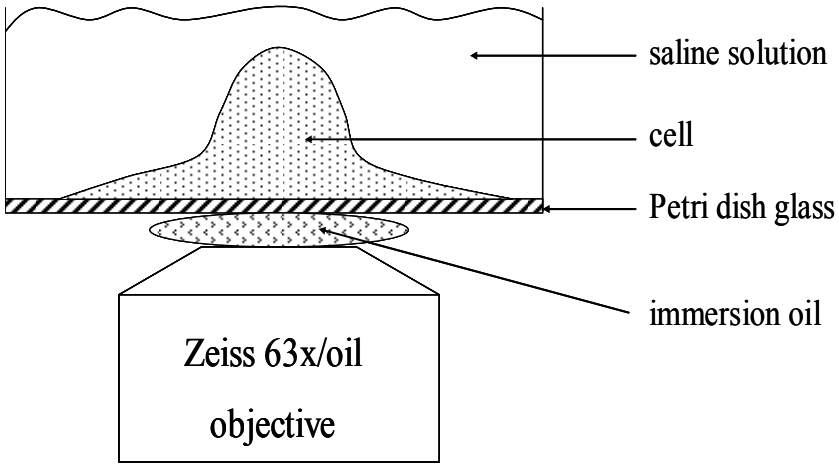

FIGURE 11 The different media along the laser beam path

The laser beam was focused by a Zeiss 63x/1.4NA Plan-Apochromat oil objective. After the objective, the laser passes through the immersion oil, Petri dish glass, cell and saline solution. The optical effect of the 0.17 mm Petri dish glass is corrected for by the objective.

To test the degree to which the spherical aberration affects our data, we turned to a simple sample. We filled a Petri dish with a solution containing the fluorophore Alexa488 and scanned our excitation beam from the bottom up into the solution. Alexa488 is a dye with an excitation wavelength of 488 nm and fluorescence emission

peaked at a wavelength of 520 nm. Because its spectrum is close to that of GFP, which has an excitation wavelength of 489 nm and emission wavelength of 508 nm, Alexa488 is often used to mimic experiments involving GFP. The dye was diluted to 8.1 nM with deionized water. We filled 0.5 mL of solution into one chamber of an eight well sample holder. The depth of the solution was approximately 0.5 cm, which is much larger than the axial size of our excitation focus spot ~1 μm. If there are no spherical aberrations, once the laser focus is completely inside the solution, the observation volume and the geometric factor γ of the laser beam would remain constant as the beam focus is moved deeper into the solution, we expected that the measurable fluorescence intensity and the Q parameter remain constant. However, the experimental result (Fig. 12) shows that there is a considerable systematic decrease in the fluorescence intensity and the Q parameter as the excitation beam penetrates deeper into the solution. Fig. 12 also shows that the expected peak of the Q parameter at the bottom edge between the glass and the solution is missing. Therefore, we propose that the missing peak in the z-scan profile of the Q parameter and the asymmetry of our cell data is mainly due to spherical aberrations coming from the mismatch of the refractive index.

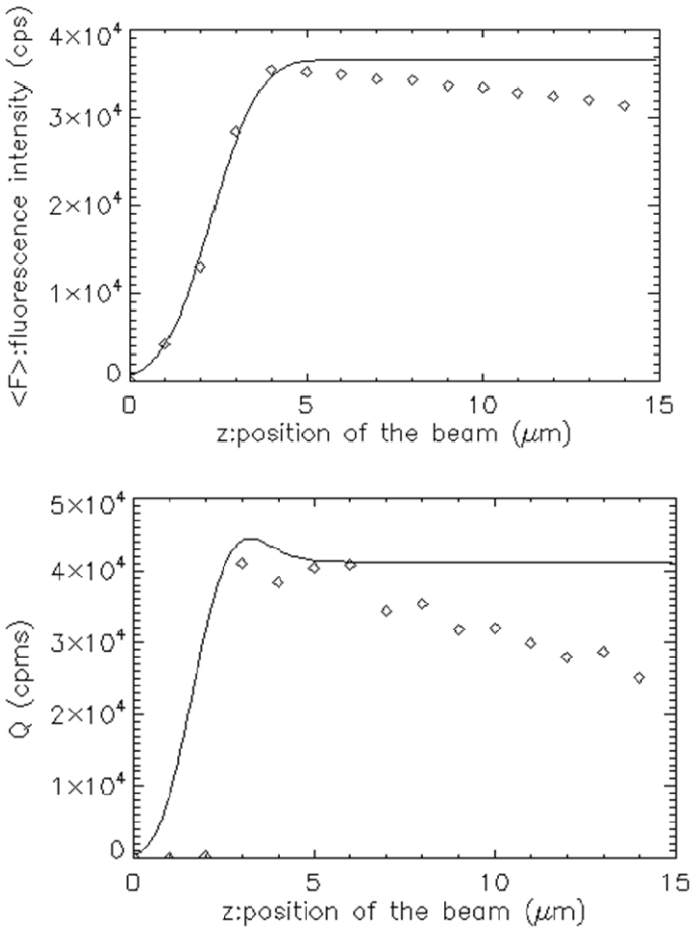

FIGURE 12 Z-scan profiles for the semi-infinite solution with an oil immersion objective

An axial scan was performed with a Zeiss 63x/1.4NA oil immersion objective across a well containing Alexa488 solution. The top graph is the fluorescence intensity and the bottom one is the Q parameter. A fit to the 3DG model recovered the distance of $h_0 = 2.3$ μm between the starting position of the scan and the surface between the glass and the solution. The 3DG model does not include spherical aberrations. The predicted intensity and the Q parameter remain the same as the excitation beam moves deep into the solution (region $h > h_0$). However, our experimental result shows that both the intensity and the Q parameter decrease as z increases. Thus, spherical aberration is severe and needs to be corrected.

3.2 Water Immersion Objective

Water immersion objectives use water as the immersion medium. These objectives are supposed to be more suitable for z-scan experiments than oil-immersion objectives because spherical aberrations due to changes in the index of refraction between the immersion medium and the sample are greatly reduced. The objective we switched to is a Zeiss 63x/1.2NA C-Apochromat water immersion objective. We performed axial scans with the water objective on the semi-infinite Alexa488 solution. Once the excitation beam was inside the solution (i.e. $z > 3$ μm, with the starting position set to $z = 0$), both the fluorescence intensity and the Mandel's Q parameter are constant for a depth of at least 15 μm (Fig. 13.).

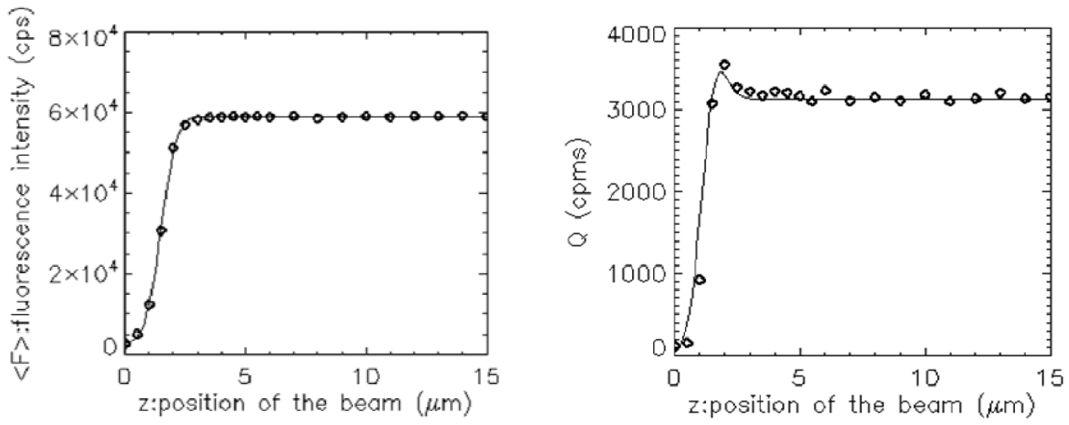

FIGURE 13 Z-profiles of a semi-infinite solution measured with a water immersion objective

Alexa488 was diluted with deionized water and put into a Petri dish. The depth of the solution was ~ 0.3 cm, which was considerably larger than the size of the excitation beam (~1 μm). An axial scan was performed with a water immersion objective. The horizontal axis is the axial position (z) of the center of the excitation beam. On the left is the fluorescence intensity in counts per second (cps); on the right is the Q parameter in counts per molecule per second (cpms). We considered that the beam was inside the solution when z > 3 μm. We measured the fluorescence intensity up to 15 μm from the starting point and calculated the corresponding Q parameter. Both <F> and Q remain constant from 3 μm to 15 μm.

We performed an axial scan on a slab containing a solution of Alexa488 with the water immersion objective. The Alexa488 slab was made by filling dye solution into the gap between a glass slide and a cover slip. It was used to model the axial-scan through a cell containing fluorescence proteins. The data reveals that both peaks in the Q parameter show up as predicted at the bottom and top edge of the slab sample. The fluorescence intensity and the Q parameter are symmetric (Fig. 14.). We fit the intensity and the Q-profile simultaneously to the 3DG model. The fit recovered an axial beam waist of 0.86 μm, a scanning offset $h_0 = 1.35$ μm and thickness of the slide $h =$ 5.20 μm. We also fit <F> and Q to the GL model and obtained $z_r =$ 0.49 μm, $h_0 = 1.32$ μm and $h =$ 5.26 μm.

The data taken with the water immersion objective are much closer to our theoretical prediction than the earlier experiments.

The water immersion objective successfully eliminates the spherical aberration problem we encountered earlier and will be used for all our axial-scan experiments. After testing the features of the water immersion objective on dye samples, we use it on cells.

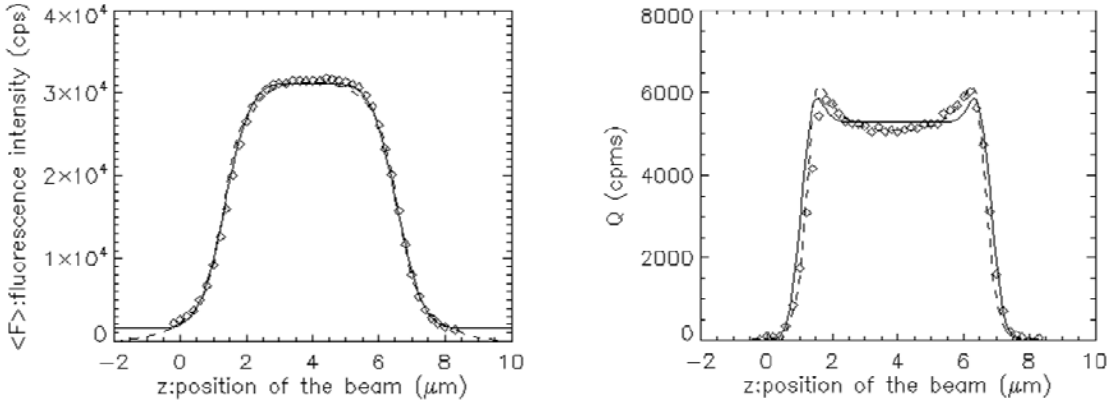

FIGURE 14 Z-scan profiles of Alexa488 slabs with water immersion objective
The fluorescence intensity is on the left in unit of cps and the Q parameter is on the right in unit of cpms. The horizontal axis is the position of the center of the excitation beam in unit of μm. Both profiles are symmetric. The data was fit to 3DG model and GL model. The recovered parameters are as follows:
3DG model (solid):
beam waist $z_0 = 0.86$ μm, z offset $h_0 = 1.35$ μm, thickness of the slide $h = 5.20$ μm.
GL model (dash):
beam waist $z_0 = 0.49$ μm, z offset $h_0 = 1.32$ μm, thickness of the slide $h = 5.26$ μm

3.3 Z-scan Experiments on Cells with the Water Immersion Objective

Cells transfected with GFP were used as samples for axial scanning with the water immersion objective. The symmetry in the fluorescence intensity and the Q parameter profiles is much improved with the new objective (Fig. 15). The data was fit to

the 3DG and the GL model. The fit (Fig. 15) recovered the physical size of the sample and the parameters of the excitation beam.

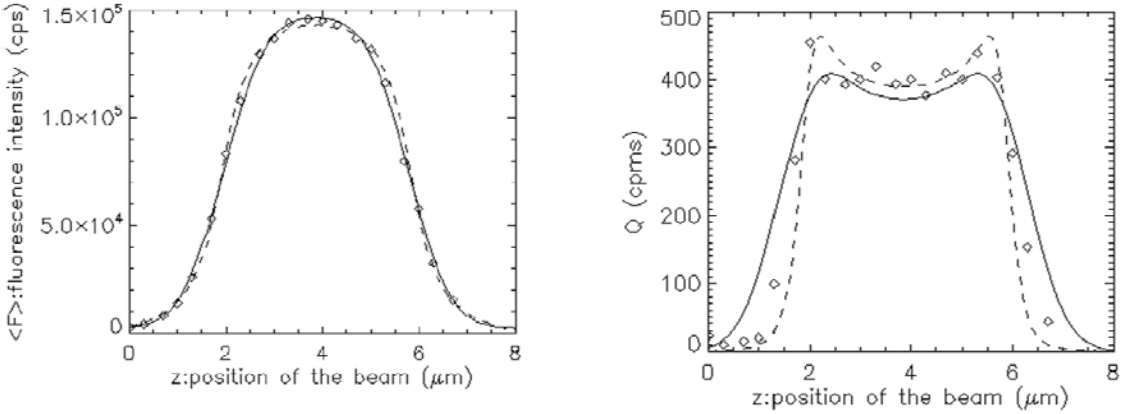

FIGURE 15 Z-scan profiles across a cell nucleus with a water immersion objective. Axial scan was performed across a GFP transfected cell nucleus. The fluorescence intensity is on the left in unit of cps and the Q parameter is on the right in unit of cpms. The horizontal axis is the position of the center of the excitation beam in unit of μm. The water immersion objective improves the data symmetry quality. The data was fit to a 3DG model and GL model. The recovered parameters are as follows:

3DG model (solid):

beam waist $z_0 = 0.98$ μm, z offset $h_0 = 1.94$ μm, thickness of the slide $h = 3.84$ μm.

GL model (dashed):

beam waist $z_r = 0.45$ μm, z offset $h_0 = 1.91$ μm, thickness of the slide $h = 3.91$ μm.

The water immersion objective eliminates the spherical aberration, and the intensity and the Q profiles are much closer to our prediction than with the oil immersion objective. However, we noticed a systematic discrepancy between the data and both models when the excitation beam is close to the boundary of the sample. In the intensity plot in Figs. 14 and 15, in regions where z < 2 μm and z > 6 μm (i.e. the excitation focus spot is only partially inside the Alexa488 sample), the 3DG model systematically

underestimates the actual intensity and the GL model overestimates the intensity. In the next chapter we introduce a model which addresses this misfit.

CHAPTER IV POINT SPREAD FUNCTION (PSF) MODELS

4.1 Comparison between Experimental Data and the Two Standard PSF Models

The most commonly used PSF models for the laser focus spot are the 3D Gaussian (3DG) model and the Gaussian-Lorentzian (GL) model. For a two-photon excitation setup, the 3DG model describes the laser intensity distribution with a PSF of Eq. (1.22) and the GL model uses Eq. (1.33). We now consider the axial-profile of the PSF, which is obtained by integrating out the radial dimension, which we refer to as radially-integrated PSF. We plot the radially-integrated PSF of the 3DG model together with a fit to the radially-integrated GL model (Fig. 16). The most distinctive difference between the two models is the faster decay of the PSF of the 3DG model with distance from the center.

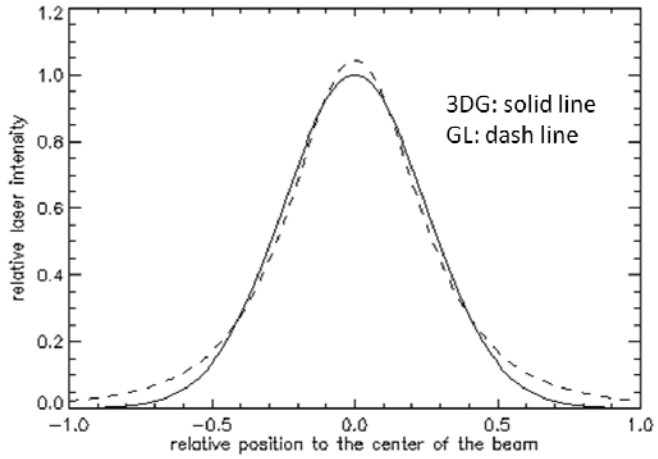

FIGURE 16 Radially-integrated PSF of the 3DG and GL model. The solid line is the axial part of PSF of the 3DG model with the axial beam waist $z_0 = 0.5$ μm. The dash line is the best fit of the 3DG model to the GL model. The tail of the 3DG axial PSF decreases rapidly. The axial PSF of the GL model has a long and gently sloped tail.

We observe the tail region in the z-scan intensity profile for the Alexa488 slide in Figs. 14 and 15. Because our data falls in between both models, an intuitive idea is to combine these two models together.

4.2 A Composite PSF Model

We define here a heuristic PSF, which will be referred to as composite PSF model. The composite PSF model has a GL function as its central part which switches over to a 3DG function at a given distance from the center. For the two-photon excitation setup, the composite PSF has the following expression.

$$PSF(\mathbf{r}) = \begin{cases} \dfrac{\omega_r^4}{\omega^4(z)} \exp\left(-\dfrac{4\left(x^2+y^2\right)}{\omega^2(z)} \right) & |z| \le L \\ A \exp\left(-\dfrac{4z^2}{z_0^2} - \dfrac{4\left(x^2+y^2\right)}{r_0^2} \right) & |z| > L \end{cases} \tag{4.1}$$

where ω_r and z_r are the radial and axial beam waists of the GL model, r_0 and z_0 are the radial and axial beam waists of the 3DG model, A is an amplitude coefficient for continuity of the fluorescence intensity and will be illustrated in the following context, and

$$\omega^2(z) = \omega_r^2 \left(1 + \left(\frac{z}{z_r} \right)^2 \right), \qquad z_r = \frac{\pi \omega_r^2}{\lambda}$$

$$S(\mathbf{r}) = \begin{cases} 1 & \text{within the sample} \\ 0 & \text{out of the sample} \end{cases}$$

We call L the cut-off length of the GL model. When the axial distance between the position of interest and the center of the excitation beam is smaller than L, the excitation laser intensity at this point of interest can be found by evaluating the GL function. When the position of interest is axially farther than L from the center of the focus spot, the laser intensity follows the 3DG function.

Suppose that we scan an excitation beam with a PSF of Eq. (4.1) across a slab of infinitesimal thickness (2D fluorescence layer), we obtain a fluorescence intensity profile

and a Q parameter profile. The fluorescent layer is located at the point $z = h_0$ and is perpendicular to the axial axis. If the position of the center of the excitation beam is denoted by the variable z, the fluorescence intensity and the Q parameter can be expressed as a function of *z*:

$$\langle F \rangle(z) = \begin{cases} \dfrac{\pi\omega_r^2}{4\left(1+\left(z-h_0\right)^2/z_r^2\right)} & |z| \le L \\ \dfrac{A\pi r_0^2}{4}\exp\left(-4\left(z-h_0\right)^2/z_0^2\right) & |z| > L \end{cases} \tag{4.2}$$

$$Q(z) = \begin{cases} \dfrac{1}{2\left(1+\left(z-h_0\right)^2/z_r^2\right)^2} & |z| \le L \\ \dfrac{A}{2}\exp\left(-4\left(z-h_0\right)^2/z_0^2\right) & |z| > L \end{cases} \tag{4.3}$$

Eqs. (4.2) and (4.3) require seven parameters to determine the intensity and Q profile: the axial beam waist z_0 of the 3DG model, the radial beam waist r_0 of the 3DG model, the axial beam waist z_r of the GL model, the radial beam waist ω_r of the GL model, the cut-off length L between the models, the coefficient *A* and the position of the sample h_0. When the continuity of $\langle F \rangle$ and Q and the differentiability of the intensity at position h_0 are imposed on the model, the numbers of parameters is reduced to four: h_0, z_r, L and the excitation wavelength λ. The first parameter relates to the sample and the rest characterize the PSF of the beam. The other parameters are related to these four parameters by,

$$z_0 = \sqrt{\frac{\lambda z_r}{\pi\left(1+\left(z-h_0\right)^2/z_r^2\right)}} \tag{4.4}$$

$$r_0 = \sqrt{4\left(z_r^2 + L^2\right)} \tag{4.5}$$

$$A = \frac{1}{\left(1+\left(L/z_r\right)^2\right)^2}\exp\left(\frac{1}{1+\left(z_r/L\right)^2}\right) \tag{4.6}$$

By changing the value of the cut-off length L, we can flexibly choose the portion of the 3DG/GL model in the composite one.

For a semi-infinite sample, which is experimentally realized by a Petri dish filled with dye solution, the sample occupation is described by the following sample geometry function $S(\mathbf{r})$.

$$S(\mathbf{r}) = \begin{cases} 1 & z \geq h_0 \\ 0 & z < h_0 \end{cases} \tag{4.7}$$

where h_0 is the edge between the solution and the Petri dish glass. The fluorescence intensity and the Q parameter can be expressed in terms of the position of the center of the excitation beam z. The fluorescence is made up of three fluorescence intensity factors ($\langle F \rangle_i$'s) and the background intensity B,

$$\langle F \rangle = \left(\langle F \rangle_1 + \langle F \rangle_2 + \langle F \rangle_3 \right) + B \tag{4.8}$$

each of them are written as:

$$\begin{aligned} \langle F \rangle_1 &= \lambda C \frac{\pi z_r^2}{4} \left[\arctan\left(z/z_r\right) + \arctan\left(\left(z - \max\left(h_0, z-L\right) \right) / z_r \right) \right] \cdot \text{step1} \\ \langle F \rangle_2 &= \lambda C \frac{\pi\sqrt{\pi}}{16} A z_0 r_0^2 \left[1 + \text{Erf}\left(2\left(z - \max\left(z+L, h_0\right) \right) / z_0 \right) \right] \\ \langle F \rangle_3 &= \lambda C \frac{\pi\sqrt{\pi}}{16} A z_0 r_0^2 \left[\text{Erf}\left(2(-L)/z_0 \right) + \text{Erf}\left(2\left(z - h_0\right)/z_0 \right) \right] \cdot \text{step3} \end{aligned} \tag{4.9}$$

where λ is the brightness per second, C is the concentration, π is the excitation wavelength, z_r is the axial beam waist for the GL section, z_0 and r_0 are the axial and radial beam waists for the 3DG section, and B indicates the background fluorescence. Mandel's Q parameter is also made up of three factors

$$Q = \frac{\langle F \rangle_1}{\langle F \rangle} Q_1 + \frac{\langle F \rangle_2}{\langle F \rangle} Q_2 + \frac{\langle F \rangle_3}{\langle F \rangle} Q_3 , \tag{4.10}$$

with each of them given by:

$$
\begin{aligned}
Q_1 &= \frac{\varepsilon \lambda z_r^2}{64}\left\{\begin{array}{l}
\dfrac{3\left(\dfrac{z-\max\left(h_0, z-L\right)}{z_r}\right)^3+5\left(\dfrac{z-\max\left(h_0, z-L\right)}{z_r}\right)}{\left(1+\left(\dfrac{z-\max\left(h_0, z-L\right)}{z_r}\right)^2\right)^2} \\
+\dfrac{3\left(\dfrac{L}{z_r}\right)^3+5\left(\dfrac{L}{z_r}\right)}{\left(1+\left(\dfrac{L}{z_r}\right)^2\right)^2} \\
+3\arctan\left(\dfrac{z-\max\left(h_0, z-L\right)}{z_r}\right) \\
+3\arctan\left(\dfrac{L}{z_r}\right)
\end{array}\right\}\cdot \text{step1} \\
Q_2 &= \varepsilon \frac{\pi\sqrt{\pi}}{32\sqrt{2}} A^2 r_0^2 z_0 \left(1+\text{Erf}\left(\frac{2\sqrt{2}\left(z-\max\left(z+L, h_0\right)\right)}{r_0}\right)\right) \\
Q_3 &= \varepsilon \frac{\pi\sqrt{\pi}}{32\sqrt{2}} A^2 r_0^2 z_0 \left(\text{Erf}\left(\frac{2\sqrt{2}\left(-L\right)}{r_0}\right)+\text{Erf}\left(\frac{2\sqrt{2}\left(z-h_0\right)}{r_0}\right)\right)\cdot \text{step3}
\end{aligned}
\tag{4.11}
$$

where the notation of the symbols are the same as previously defined in this thesis; step1 and step3 are step functions defined as follows:

$$
\begin{aligned}
\text{step1} &= \begin{cases} 1 & z+L > h_0 \\ 0 & z+L \le h_0 \end{cases} \\
\text{step3} &= \begin{cases} 1 & z-L > h_0 \\ 0 & z-L \le h_0 \end{cases}
\end{aligned}
\tag{4.12}
$$

For a slab sample which has axial boundaries at h_0 and $h_0 + h$ with the corresponding sample geometry function

$$
S\left(\mathbf{r}\right) = \begin{cases} 1 & h_0 < z < h_0 + h \\ 0 & \text{otherwise} \end{cases}
\tag{4.13}
$$

we obtain the intensity and Q function through integration of Eq. (1.4) and Eq. (1.14). The total fluorescence intensity is the addition of three factors and the background signal.

$$\langle F\rangle = \langle F\rangle_1 + \langle F\rangle_2 + \langle F\rangle_3 + B \tag{4.14}$$

$$\langle F\rangle_1 = \lambda C \frac{\pi z_r^2}{4}\left(\arctan\left(\frac{\min\left(h_0+h, z+L\right)-z}{z_r}\right)+\arctan\left(\frac{z-\max\left(h_0, z-L\right)}{z_r}\right)\right)\cdot \text{step1}$$

$$\langle F\rangle_2 = \lambda C \frac{\pi\sqrt{\pi}Ar_0^2 z_0}{16}\left(\text{Erf}\left(\frac{2\left(z-h_0\right)}{z_0}\right)+\text{Erf}\left(\frac{2\left(\min\left(h_0+h, z-L\right)-z\right)}{z_0}\right)\right)\cdot \text{step2} \tag{4.15}$$

$$\langle F\rangle_3 = \lambda C \frac{\pi\sqrt{\pi}Ar_0^2 z_0}{16}\left(\text{Erf}\left(\frac{2\left(z-\max\left(h_0, z+L\right)\right)}{z_0}\right)+\text{Erf}\left(\frac{2\left(h_0+h-z\right)}{z_0}\right)\right)\cdot \text{step3}$$

The Q function is

$$Q = \frac{\langle F\rangle_1}{\langle F\rangle}Q_1 + \frac{\langle F\rangle_2}{\langle F\rangle}Q_2 + \frac{\langle F\rangle_3}{\langle F\rangle}Q_3 \tag{4.16}$$

where Q_1, Q_2 and Q_3 are written as:

$$Q_1 = \frac{\varepsilon \lambda z_r^2}{64}\left\{\begin{array}{l} \dfrac{3\left(\dfrac{z-\max\left(h_0, z-L\right)}{z_r}\right)^3 + 5\left(\dfrac{z-\max\left(h_0, z-L\right)}{z_r}\right)}{\left(1+\left(\dfrac{z-\max\left(h_0, z-L\right)}{z_r}\right)^2\right)^2} \\ + \dfrac{3\left(\dfrac{\min\left(h_0+h, z+L\right)-z}{z_r}\right)^3 + 5\left(\dfrac{\min\left(h_0+h, z+L\right)-z}{z_r}\right)}{\left(1+\left(\dfrac{\min\left(h_0+h, z+L\right)-z}{z_r}\right)^2\right)^2} \\ +3\arctan\left(\dfrac{z-\max\left(h_0, z-L\right)}{z_r}\right) \\ +3\arctan\left(\dfrac{\min\left(h_0+h, z+L\right)-z}{z_r}\right) \end{array}\right\}\cdot \text{step1}$$

$$Q_2 = \varepsilon \frac{\pi\sqrt{\pi}}{32\sqrt{2}} A^2 r_0^2 z_0 \left(\text{Erf}\left(\frac{2\sqrt{2}\left(z-h_0\right)}{z_0}\right) + \text{Erf}\left(\frac{2\sqrt{2}\left(\min\left(h_0+h, z-L\right)-z\right)}{z_0}\right)\right)\cdot \text{step2} \quad (4.17)$$

$$Q_3 = \varepsilon \frac{\pi\sqrt{\pi}}{32\sqrt{2}} A^2 r_0^2 z_0 \left(\text{Erf}\left(\frac{2\sqrt{2}\left(z-\max\left(h_0, z+L\right)\right)}{z_0}\right) + \text{Erf}\left(\frac{2\sqrt{2}\left(h_0+h-z\right)}{z_0}\right)\right)\cdot \text{step3}$$

Step functions step1, step2 and step3 are defined by

$$\text{step1} = \begin{cases} 1 & \min\left(h_0+h, z+L\right) > \max\left(h_0, z-L\right) \\ 0 & \text{otherwise} \end{cases}$$

$$\text{step2} = \begin{cases} 1 & z-L > h_0 \\ 0 & \text{otherwise} \end{cases} \quad (4.18)$$

$$\text{step3} = \begin{cases} 1 & h_0+h > z+L \\ 0 & \text{otherwise} \end{cases}$$

4.3 Results

With the analytical expression for the intensity and the Q parameter for the composite model, we are ready to refit the axial scan data of the slab samples. Fig. 17 shows the z-scan profiles of the Alexa488 slide, the global fit to the composite model and

the relative residuals. The fit recovers the parameters for the configuration of the excitation beam, the geometry parameters and the molecular parameters of the sample: axial beam waist of the GL model $z_r = 0.49$ μm, cut-off length $L = 1.57$ μm, axial offset $h_0 = 1.35$ μm, slab's thickness $h = 5.20$ μm, the molecular brightness of the Alexa488 dye ε = 23000 cpms. The quality of the fit curve is greatly improved by the composite model. The overestimation and underestimation that occurred with the GL and the 3DG model are not apparent when using the composite model.

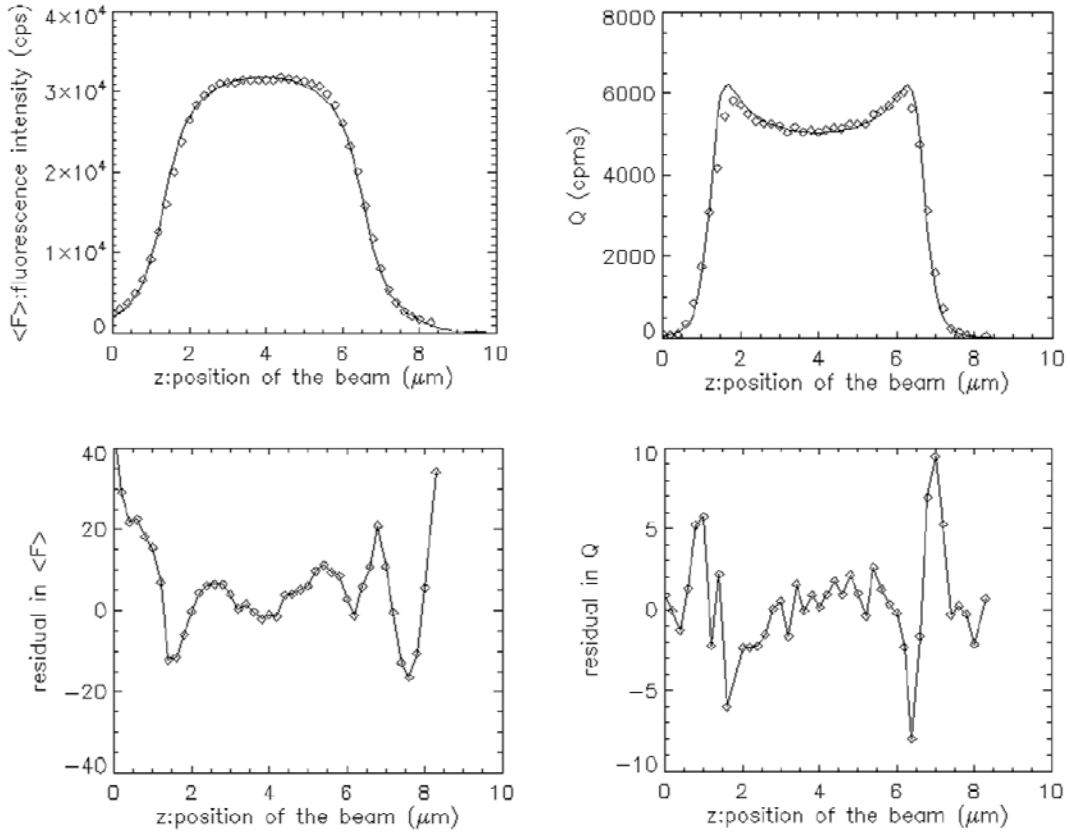

FIGURE 17 Z-scan intensity and Q profiles of Alexa488 slide were fit to the composite model.

Alexa488 solution was filled into the gap between a glass slide and a cover slip. An axial scan was performed across this dye slab. At each step, the fluorescence intensity was measured and the Q parameter was calculated. The plotted $\langle F \rangle$ is in cps. Q is in cpms. They were simultaneously fit to the composite model. The axial offset is 1.35 μm, the thickness of the slab is 5.20 μm, the axial beam waist of the GL model is 0.49 μm, and the cut-off length between models is 1.57 μm. The relative residuals between the data and the fitted curved are plotted beneath the data.

The composite model was also applied to the cell data. The same data as in Fig. 15. was fit to the composite slab model. The result is shown in Fig. 18. The

recovered parameters are: GL model's axial beam waist z_r = 0.45 μm, cut-off length L = 1.33 μm, z offset h_0 = 1.91 μm, slab thickness h = 3.92 μm, molecular brightness ε = 1660 cpms, and concentration C = 1.17 μM.

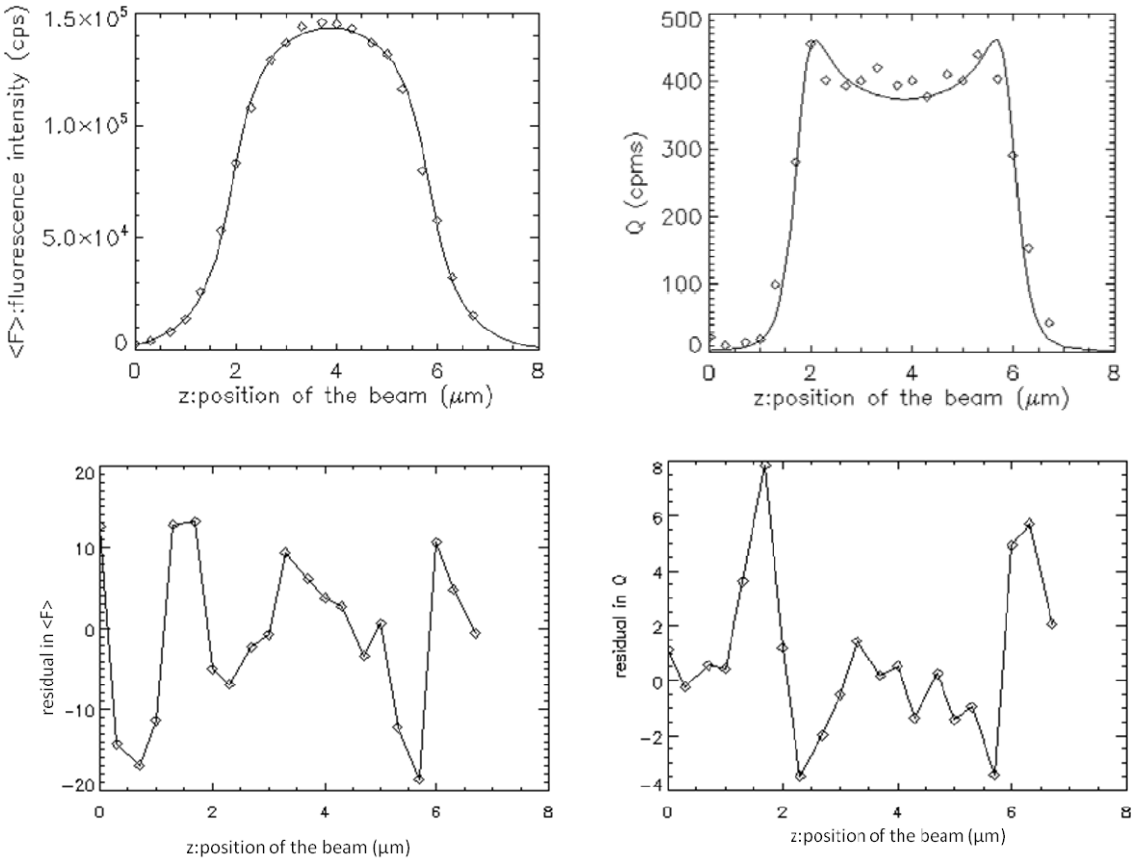

FIGURE 18 Z-scan intensity and Q profiles across cell nucleus were fit to the composite model.

The nuclear section of a GFP transfected cell was measured. The fluorescence intensity $\langle F \rangle$ is in cps and the Q is in cpms. They are fit simultaneously to the composite model. The model recovers the GL model's axial beam waist z_r = 0.45 μm, the cut-off length L = 1.33 μm, the z offset h_0 = 1.91 μm, the slab thickness h = 3.92 μm, the molecular brightness ε = 1660 cpms, and the concentration C = 1.17 μM. The relative residuals are plotted beneath the data and the fits.

The composite model effectively abolishes the large systematic misfit at the edges of the slab as observed for the GL and 3DG model. However, a closer look reveals that

the relative residuals of the fluorescence intensity and Q-parameter fit are very high at the edges of the sample slab, which results in a large reduced chi square value of the fit. The relative residual is determined by the ratio of the difference between the fit value and the data to the experimental error of the data. Theory predicts that the experimental error of the fluorescence intensity at each step is supposed to be quite small [18]. A large relative residual may arise from the incorrect determination of the experimental error. Therefore, we investigate the uncertainty of the measurement in the next chapter.

CHAPTER V STABILITY OF THE AXIAL-SCAN FFS MEASUREMENT

5.1 The Experimental Error of the Fluorescence Intensity

We mentioned at the end of the last chapter that the relative residual of the fluorescence intensity is large. Because the relative residual of a physical quantity is inversely proportional to its experimental error, the determination of the experimental error is important. We investigate this issue in this chapter.

The experimental error was obtained as in the following. For cell measurement, at each step of the scan we took data at 20 kHz for 20 cycles. Each cycle stores 32768 successive data points. The whole measurement had 655360 data points and lasted 33 s. We divided the data into 20 segments, each of which was equivalent to a cycle. We consider these 20 intensities as our sample space. The mean value and the standard deviation of these 20 intensities were calculated. The standard error of the mean intensity value is estimated by the sample standard deviation divided by the square root of the sample size. If there is no additional error besides the statistical error, then the mean and the standard error calculated by the above procedure characterize the experimental data.

To test the reliability of obtaining faithful experimental errors by the above method, we kept the instrumentation and the measuring procedure the same as before. However, instead of scanning the beam across the sample once, we scanned across the same sample multiple times. After scanning the beam up across the cell nucleus, we moved the beam down to its starting position and rescanned it up again at the same position. We expect the axial profile for the intensity to be the same for all scans. While two successive scanning profiles overlap (Fig. 19), there is a systematic shift between

these two profiles. This could be due to either cell movement or mechanical drift of the instrument.

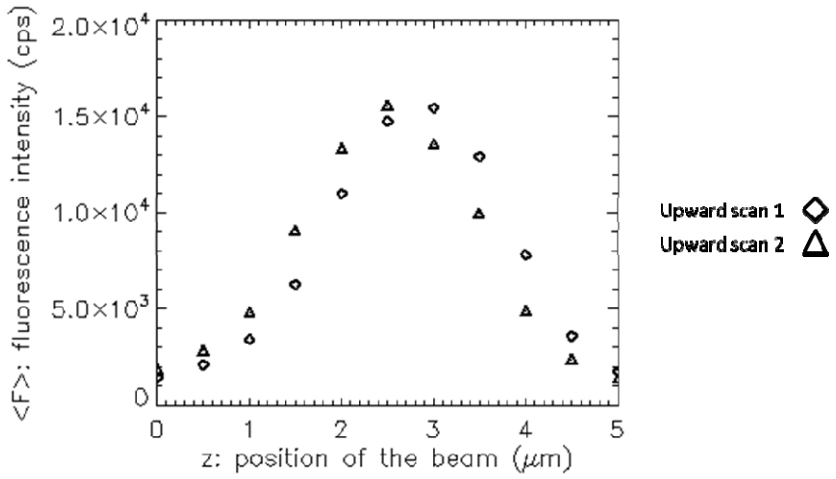

FIGURE 19 Successive axial scan across the cell nucleus

Two axial scans were performed at the same radial position at the cytoplasm of a COS cell transfected with GFP. There is an obvious shift along the z direction between two successive scanning profiles.

To tell whether the right shift of the data in Fig. 19 was caused by cell movement or by mechanical drift of the measuring apparatus, we returned to the simplest system at hand: the semi-infinite dye solution- a Petri dish filled with Alexa488 solution with thickness of ~ 0.5 cm. We scanned the excitation beam twice through the sample. An apparent shift between the two scanning profiles was observed (Fig. 20). Hence, we conclude that the non-repeatability of the scans is related to mechanical drifts rather than cell movement.

Suppose we measure at position z = 1.79 μm in Fig. 20, we obtain either an intensity of 38240 cps (diamond) or an intensity of 53250 cps (triangle). The difference between these two values is 15010 cps, approximately 40% of 38240 cps. If we perform 20 scans and calculate the experimental error at this position using the 20 intensities of these 20 scans, the percentage experimental error is 40%. However, if we used the

information of a single data point (at 1.79 μm with 38240 cps), chop the data into 50 segments (the dye measurements were taken at 50 kHz for 50 cycles) and calculate the mean and the standard error of the mean. The statistical standard error is 0.3%. With 40% being much larger than 0.3%; the actual experimental error is much larger than that calculated by our original method.

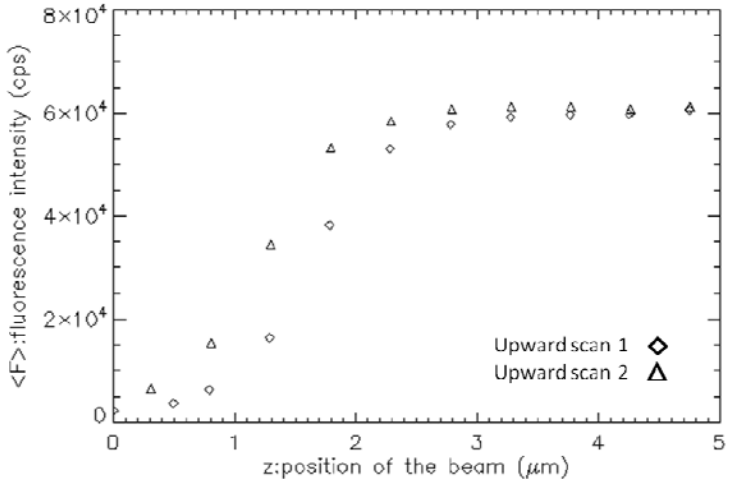

FIGURE 20 Two successive upward scans across an Alexa488 solution in an eight well

Two successive scans were performed under identical conditions and at the same lateral position. The horizontal axis is the position of the focus beam in units of μm. The vertical axis is the fluorescence intensity in units of cps. The axial profiles of <F> for two successive scans do not overlap.

The results in Fig. 19 and 20 indicate a large experimental error in the fluorescence intensity. It also tells us that such large errors are mostly due to mechanical drift which alters the separation between the objective and the sample with time.

There are several potential weak links in our experimental setup. First, the Petri dish was put on top of the microscope without firmly fastening it. There may be wobbling of the Petri dish when the objective is moved up and down. Second, because we use a

water immersion objective, the objective and the bottom surface of the Petri dish are mechanically coupled by the water. If the water dried out along with time, there would be potentially a small relative movement between the objective and the sample. Third, the objective was raised and lowered by the mechanics of the microscope, which could introduce slippage, backlash or drift. Fourth, external factors, such as temperature drifts, mechanical vibrations of motors, and handling of the experimental setup by the experimentalist are potential sources of concern.

5.2 Stability of the Stage

In our experiment, the Petri dish sits on top of the sample holder of a Piezo stage. The Piezo stage is fixed to the microscope by screws, but the sample holder is attached to the Piezo stage with spring clamps only. Because we use a water immersion objective which has direct contact with the Petri dish, the dish may wobble when the objective pushes and pulls at the Petri dish. The lighter the Petri dish, the easier this situation may occur. Therefore, we fixed the Petri dish to a heavy home-made sample holder to prevent wobble. At the same time, we had to limit the scanning motion to a small range to prevent a potential mechanical crash between the objective and the sample, which would damage the very expensive objective.

5.3 Immersion Medium

We switched from oil immersion to water immersion objectives because water objectives suffer fewer aberrations. However, water evaporates much faster than oil. If water evaporates, the mass pulling on the thin coverslip is gone which may change the distance between the objective and the sample. To test whether water evaporation is a potential problem, we used an air objective to carry out similar experiments as shown in Fig. 20. We scanned the excitation beam focused by a Zeiss 20x/0.75NA air objective across an Alexa488 semi-infinite solution. The experiment demonstrates that an axial shift between two successive scans is still observed (Fig. 21). The mechanical drift has to be caused by other factors.

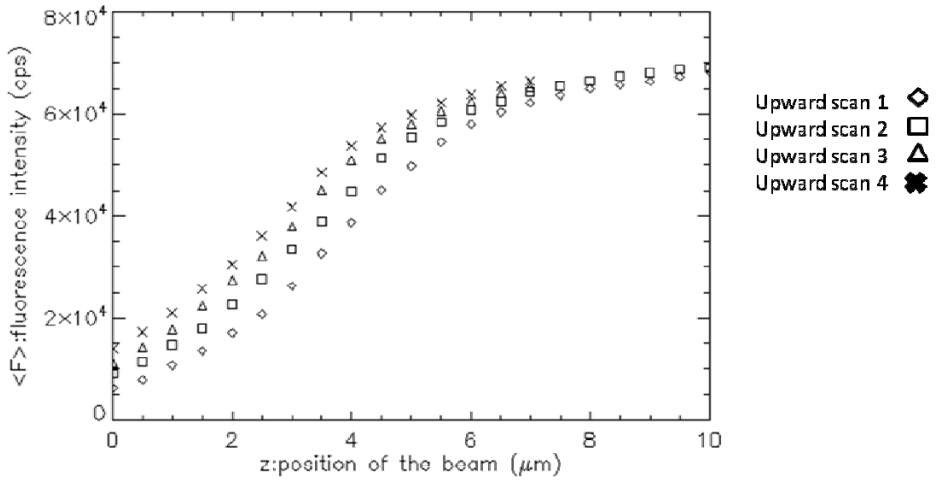

FIGURE 21 Intensity profiles of successive scans across Alexa488 in an eight-well chamber slide with an air objective

Axial scans were performed at a fixed lateral position across the Alexa488 semi-infinite sample. A Zeiss 20x/0.75NA air objective was used. When a scan was finished, the excitation beam was moved to its starting position for another identical scan. Four upward scans were taken in sequence (diamonds, squares, triangles and crosses). There is a systematic left shift of the curves between successive scans.

5.4 Stability of the Microscope

Although the numerical apertures of the current existing air objectives are too low to carry out FFS experiments, the air objective is ideal for testing the presence of drifts caused by the microscope mechanics, because the objective has no physical contact with the Petri dish. We took a long measurement with the air objective at a point near the bottom edge of the semi-infinite Alexa488 sample. Meanwhile, we monitored the stability of the Piezo stage and confirmed that its motion is less than 10 nm. We consistently observed a continuous increase in the fluorescence intensity, which indicates a relative movement between the objective and the stage. Representative data

demonstrating an increasing intensity is shown in Fig. 22 (a). We suspect that the internal mechanics which drives the objective's vertical motion is not stable so that the same experiment was carried out on another newer microscope multiple times on multiple days. This experiment also identified intensity fluctuation in long measurements. But unlike the first microscope there is no monotonic increase in intensity (representative data is shown in Fig. 22 (b)). We conclude from these experiments that the main source of instability is the microscope itself. A method that monitors the position of the objective and keeps it stable would be very beneficial for axial-scan FFS.

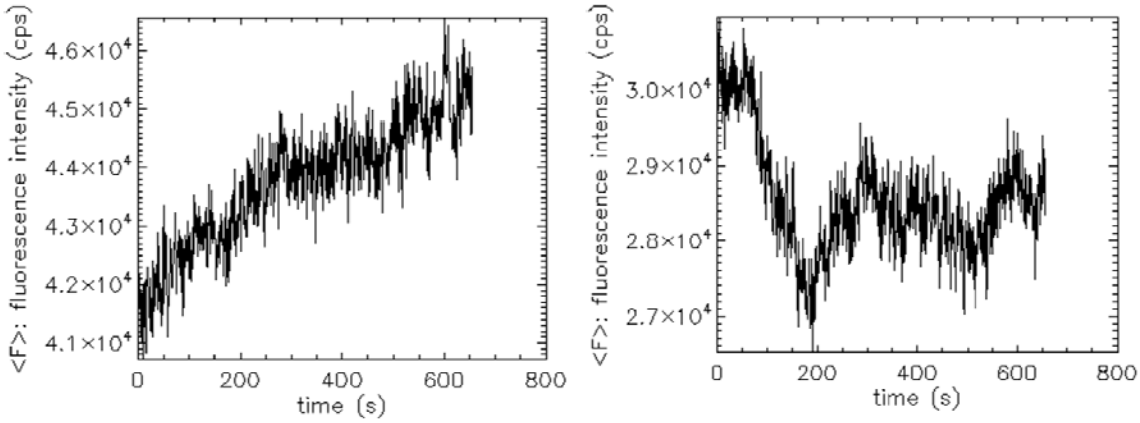

(a) (b)

FIGURE 22 Intensity trails along with time at the edge of Alexa488 solution The excitation beam was focus at the bottom edge of Alexa488 semi-infinite sample with an air objective. (a) Experiment was carried out on a older microscope. (b) Experiment was performed on a newer one.

5.5 Slow Scan versus Fast Scan

We spent approximately 30 s to gather information at each step of the z scans in all experiments described in this thesis. A complete scan takes up to half an hour when the times to manually changing the axial position of the beam were all taken into account. The longer it takes to perform a complete scan, the more likely it is to observe a

significant drift of the beam position. Reducing the measurement time is a potential solution to this problem. However, a shorter measurement may not have sufficient signal to noise to effectively calculate fluctuation parameters. A potential solution is to take multiple fast scans along the same axis, align the fast scans to eliminate drift, and correlate the data points across the aligned scans. This method is currently under development in our lab.

CHAPTER VI SUMMARY

We encountered a number of obstacles while developing axial-scan FFS. Spherical aberrations affect the quality of the z-scan data, which was overcome by using a water immersion objective. We also discovered that by combining the GL and the 3DG PSF models we describe the z-scan data much more accurately. We further realized that z-scans measurements are not repeatable due to the presence of drifts. We investigated potential processes that could account for the observed drift and concluded that the limited mechanical stability of the microscope itself is the source of the problem. It will be imperative to improve the stability of the experimental setup in order to perform successful axial-scan FFS experiments. This thesis describes the first steps of developing axial-scan FFS. Further improvements and method development will be required to transform axial-scan FFS into a robust method suitable for cellular applications.

References

1. Gheysen, D. *et al*. Assembly and release of HIV-1 precursor Pr55gag virus-like particles from recombinant baculovirus-infected insect cells. *Cell* **59**, 103-112 (1989).

2. Yeager, M., Wilson-Kubalek, E. M., Weiner, S. G., Brown, P. O. & Rein, A. Supramolecular organization of immature and mature murine leukemia virus revealed by electron cryo-microscopy: implications for retroviral assembly mechanisms. *Proc. Natl. Acad. Sci. U. S. A.* **95**, 7299-7304 (1998).

3. Li, S., Hill, C. P., Sundquist, W. I. & Finch, J. T. Image reconstructions of helical assemblies of the HIV-1 CA protein. *Nature* **407**, 409-413 (2000).

4. Chen, Y., Wu, B., Musier-Forsyth, K., Mansky, L. M. & Mueller, J. D. Fluorescence fluctuation spectroscopy on viral-like particles reveals variable gag stoichiometry. *Biophys. J.* **96**, 1961-1969 (2009).

5. Murray Stewart. Insight into the Molecular Mechanism of Nuclear Trafficking Using Nuclear Transport Factor 2 (NTF2). *Cell Structure and Function* **25**, 217 (2000).

6. Ribbeck, K., Lipowsky, G., Kent, H. M., Stewart, M. & Gorlich, D. NTF2 mediates nuclear import of Ran. *EMBO J.* **17**, 6587-6598 (1998).

7. Chen, Y., Wei, L. N. & Muller, J. D. Unraveling protein-protein interactions in living cells with fluorescence fluctuation brightness analysis. *Biophys. J.* **88**, 4366-4377 (2005).

8. Chen, Y., Wei, L. N. & Muller, J. D. Probing protein oligomerization in living cells with fluorescence fluctuation spectroscopy. *Proc. Natl. Acad. Sci. U. S. A.* **100**, 15492-15497 (2003).

9. Chen, Y. & Muller, J. D. Determining the stoichiometry of protein heterocomplexes in living cells with fluorescence fluctuation spectroscopy. *Proc. Natl. Acad. Sci. U. S. A.* **104**, 3147-3152 (2007).

10. Chen, Y., Muller, J. D., Berland, K. M. & Gratton, E. Fluorescence fluctuation spectroscopy. *Methods* **19**, 234-252 (1999).

11. Thompson, N. L., Lieto, A. M. & Allen, N. W. Recent advances in fluorescence correlation spectroscopy. *Curr. Opin. Struct. Biol.* **12**, 634-641 (2002).

12. Denk, W., Strickler, J. H. & Webb, W. W. Two-photon laser scanning fluorescence microscopy. *Science* **248**, 73-76 (1990).

13. Elson, E. L. Quick tour of fluorescence correlation spectroscopy from its inception. *J. Biomed. Opt.* **9**, 857-864 (2004).

14. Meseth, U., Wohland, T., Rigler, R. & Vogel, H. Resolution of fluorescence correlation measurements. *Biophys. J.* **76**, 1619-1631 (1999).

15. Chen, Y., Muller, J. D., So, P. T. & Gratton, E. The photon counting histogram in fluorescence fluctuation spectroscopy. *Biophys. J.* **77**, 553-567 (1999).

16. Thompson, N. L. in *Topics in Fluorescence Spectroscopy* (ed Lakowicz, J. R.) (Plenum Press, New York, 1991).

17. Mandel L. Sub-Poissonian photon statistics in resonance fluorescence. *Optics Letters* **4**, 205 (1979).

18. Wu, B. & Muller, J. D. Time-integrated fluorescence cumulant analysis in fluorescence fluctuation spectroscopy. *Biophys. J.* **89**, 2721-2735 (2005).

19. Sanchez-Andres, A., Chen, Y. & Muller, J. D. Molecular brightness determined from a generalized form of Mandel's Q-parameter. *Biophys. J.* **89**, 3531-3547 (2005).

20. Berland, K. M., So, P. T. & Gratton, E. Two-photon fluorescence correlation spectroscopy: method and application to the intracellular environment. *Biophys. J.* **68**, 694-701 (1995).